



# Supersonic impact resilience of nanoarchitected carbon

Carlos M. Portela<sup>1</sup>✉, Bryce W. Edwards<sup>2</sup>, David Veysset<sup>1,3,7</sup>, Yuchen Sun<sup>3,4</sup>, Keith A. Nelson<sup>1,3,4</sup>, Dennis M. Kochmann<sup>1,5</sup> and Julia R. Greer<sup>1,2,6</sup>✉

Architected materials with nanoscale features have enabled extreme combinations of properties by exploiting the ultralight-weight structural design space together with size-induced mechanical enhancement at small scales. Apart from linear waves in metamaterials, this principle has been restricted to quasi-static properties or to low-speed phenomena, leaving nanoarchitected materials under extreme dynamic conditions largely unexplored. Here, using supersonic microparticle impact experiments, we demonstrate extreme impact energy dissipation in three-dimensional nanoarchitected carbon materials that exhibit mass-normalized energy dissipation superior to that of traditional impact-resistant materials such as steel, aluminium, polymethyl methacrylate and Kevlar. In-situ ultrahigh-speed imaging and post-mortem confocal microscopy reveal consistent mechanisms such as compaction cratering and microparticle capture that enable this superior response. By analogy to planetary impact, we introduce predictive tools for crater formation in these materials using dimensional analysis. These results substantially uncover the dynamic regime over which nanoarchitecture enables the design of ultralightweight, impact-resistant materials that could open the way to design principles for lightweight armour, protective coatings and blast-resistant shields for sensitive electronics.

Historically, the ability of a material to accommodate specific loading conditions has been linked to its ordering from the nanoscale (for example, an atomic crystal structure), to the microscale (for example, a grain distribution) and ultimately to the macroscale structural form factor, but only recently has the design parameter space drastically broadened at the nano- to microscales. An example of this progress has been the use of nano- and micro-architecture in materials, which has opened a regime of mechanical properties previously unattainable by homogeneous materials. Using natural materials as inspiration, several micro- and nanoarchitected materials have been realized with unique combinations of mechanical properties such as high stiffness-to-weight and strength-to-weight ratios<sup>1,2</sup>, extreme resilience<sup>3</sup> and reversible energy absorption<sup>4</sup>. Despite these achievements, explorations have focused on the static regime, leaving the dynamic parameter space largely unexplored. Several works have ventured beyond statics into the propagation of waves in these materials, showing the formation of acoustic band gaps<sup>5</sup> and polarized wave propagation<sup>6</sup>, while being restricted to small-displacement, reversible deformation. Explorations in large-amplitude dynamic regimes, for instance, have been essential to determine the equations of state<sup>7</sup>—and thus develop a full physical understanding—of homogeneous materials such as metals, polymers and ceramics, but are still lacking in the novel material systems described above. In light of this, the promising prospects for these materials have yet to be fully unveiled because many proposed applications, ranging from protection against low-energy impulsive loads<sup>8</sup> to shielding against shock and blast<sup>9</sup>, lie beyond small deformations and quasi-statics.

In the search for efficient blast- and impact-protecting materials, studies on the dynamic response of stochastic heterogeneous materials

such as open- and closed-cell foams<sup>10,11</sup> paved the way for explorations of macroscale architected materials for ballistic impact<sup>12</sup> or blast<sup>13</sup>. Similarly to their stochastic counterparts, macroscale dynamic experiments and simulations<sup>14</sup> of three-dimensional (3D) lattice materials have elucidated the benefits of this architecture for energy absorption in regimes ranging from low-velocity drop-weight experiments<sup>15</sup> to faster Hopkinson-bar-type compressions<sup>16–18</sup>, where shock-wave propagation has been observed<sup>11,17</sup>. At the microscale, recent works on polymeric architectures have also reported energy dissipation mechanisms such as strut buckling at low velocities<sup>19</sup> and, at higher velocities, evidence of compaction shocks<sup>20</sup> has also been observed. Understanding and translating these dynamic properties to the micro- and nanoarchitected scale is not only necessary for a variety of applications that require miniaturization of these materials<sup>9</sup>, but is also highly desirable due to the possibility of harnessing material size effects, as recently demonstrated for impacts on nanoscale graphene<sup>21</sup> and polystyrene<sup>22</sup> films. Although size effects have been widely explored quasi-statically, their effect in the dynamic realm remains to be uncovered; these effects have the potential to introduce extreme energy absorption capabilities to already efficient architectures.

Here we combine two previously independent and largely unexplored concepts—3D nanoarchitectures under supersonic impact and material size effects under extreme dynamic loading—as a route to develop advanced structural metamaterials with simultaneous low weight, high stiffness and extreme specific energy dissipation. We fabricate, test and analyse 3D nanoarchitected carbon lattice materials composed of 13,500 unit cells with beam diameters ranging from ~370 to ~530 nm and relative densities (that is, fill fractions) ranging from ~14% to ~23% under supersonic

<sup>1</sup>Department of Mechanical Engineering, Massachusetts Institute of Technology, Cambridge, MA, USA. <sup>2</sup>Division of Engineering and Applied Science, California Institute of Technology, Pasadena, CA, USA. <sup>3</sup>Institute for Soldier Nanotechnologies, Massachusetts Institute of Technology, Cambridge, MA, USA. <sup>4</sup>Department of Chemistry, Massachusetts Institute of Technology, Cambridge, MA, USA. <sup>5</sup>Department of Mechanical and Process Engineering, ETH Zürich, Zürich, Switzerland. <sup>6</sup>The Kavli Nanoscience Institute at Caltech, Pasadena, CA, USA. <sup>7</sup>Present address: Hansen Experimental Physics Laboratory, Stanford University, Stanford, CA, USA. ✉e-mail: [cportela@mit.edu](mailto:cportela@mit.edu); [jrreer@caltech.edu](mailto:jrreer@caltech.edu)

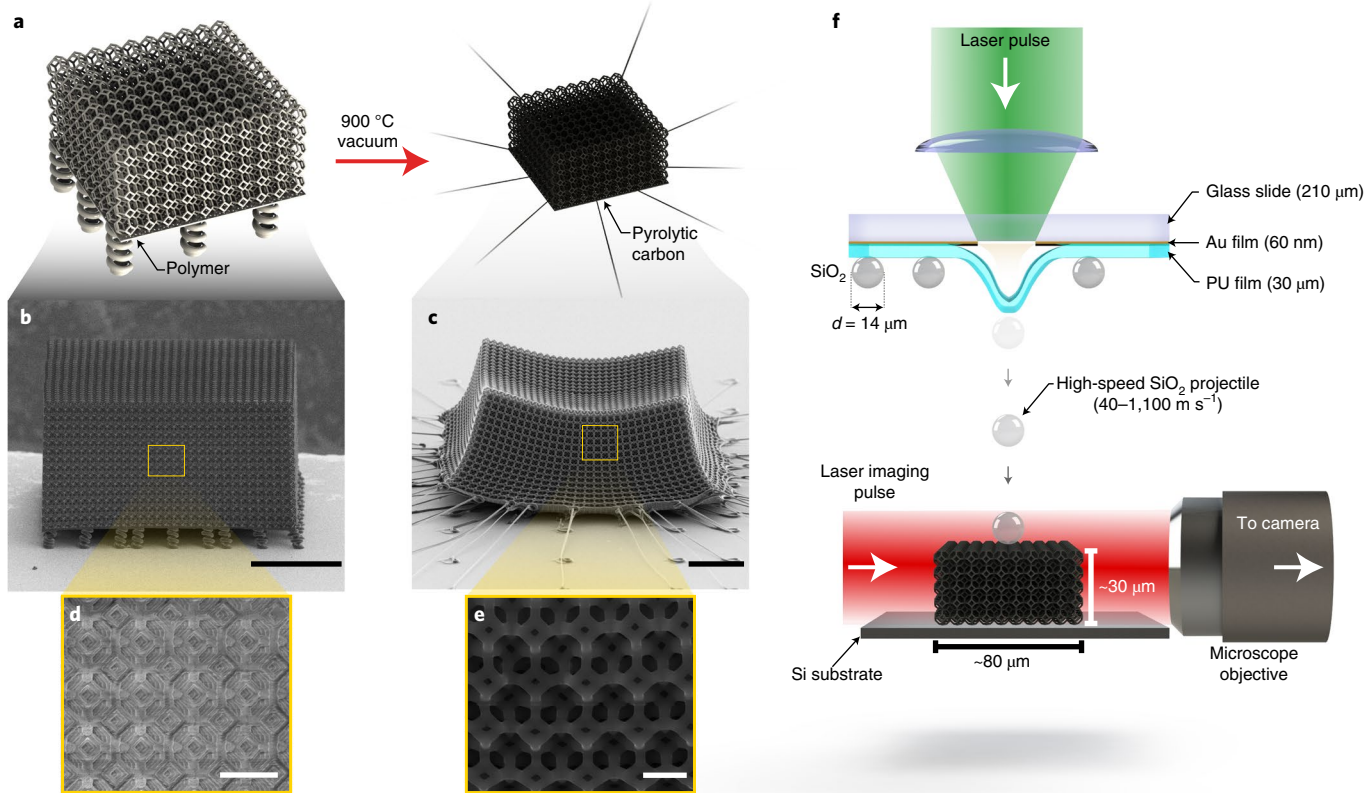


**Fig. 1 | Material fabrication and microparticle impact experiments.** **a**, Diagram of the fabrication process: the 3D-patterned IP-Dip tetrakaidecahedron material supported by helical springs converts to a pyrolytic carbon replica, shrunk by ~75% in each dimension, tethered to the substrate by nanowires resulting from stretched springs. **b,c**, SEM micrographs of an IP-Dip precursor sample (**b**) and the resulting pyrolytic carbon sample (**c**). **d,e**, Higher-magnification micrographs showing unit cell details of the samples in **b** and **c**. **f**, Schematic (not to scale) of the LIPIT showing the Au ablation process imparting kinetic energy to the  $\text{SiO}_2$  projectile, whose impact with the target material is captured using an ultrahigh frame rate camera. PU, polyurea. Scale bar, 100  $\mu\text{m}$  (**b**), 20  $\mu\text{m}$  (**c**), 10  $\mu\text{m}$  (**d**) and 2  $\mu\text{m}$  (**e**).

microparticle impact, and compare their superior responses to those of classic ballistic materials. We use the laser-induced particle impact test (LIPIT) to accelerate microscopic spherical projectiles toward our materials while employing ultrahigh-speed imaging to capture the impact process in real time, with micrometre and nanosecond resolution, along with laser-confocal and electron microscopy post-mortem techniques to qualitatively and quantitatively describe the observed response. Using relative density and impact energy as input parameters, we establish their effects on the failure process and energy absorption capabilities of these nanoarchitected carbon materials. To understand and predict their ballistic response, we utilize concepts from dimensional analysis of planetary impact, allowing predictive tools to be drawn from a physically similar (albeit dimensionally different) problem while shedding light on this unexplored realm for architected materials.

We fabricated 3D nanoarchitected materials by first patterning predesigned cross-linked polymer structures out of IP-Dip photore sist using two-photon lithography and subsequently pyrolysing these structures in vacuum to 900  $^{\circ}\text{C}$ <sup>2,23</sup>. This process produced pyrolytic carbon replicas of the original architectures, isotropically shrunk by ~75% (Fig. 1). We selected a tetrakaidecahedral underlying architecture, initially motivated by this structure's bending-dominated response<sup>1,24</sup>, which leads to non-catastrophic failure and lacks a softening post-yield behaviour in the quasi-static regime<sup>25</sup>. Additionally, this architecture's relatively constant collapse stress (also comparable to the initial yield stress) provided another benefit for impact energy absorption<sup>26,27</sup>. While the quasi-static properties of tetrakaidecahedra do not directly translate to extreme

dynamic regimes such as the ones in this work, where structural guiding principles are still lacking, some of its beneficial characteristics have indeed been shown to hold in dynamic regimes<sup>14</sup>. To achieve a proper separation of scales between unit cell size and the overall sample dimensions, each sample consisted of a sufficiently large tessellation of  $30 \times 30 \times 15$  unit cells (Extended Data Fig. 1). With the objective of probing the effect of fill fraction on the impact response, we fabricated samples of two relative densities  $\bar{\rho} = 14\% \pm 2\%$  and  $23\% \pm 3\%$  by varying the pyrolytic carbon strut diameter between  $d = 370 \pm 40 \text{ nm}$  and  $530 \pm 40 \text{ nm}$  while maintaining the unit cell size at  $2.5 \pm 0.2 \mu\text{m}$ . By achieving these nanoscale strut dimensions, the structures fall within the size-effect regime for pyrolytic carbon, where it exhibits a rubber-like response prior to brittle failure, possesses an extended elastic regime (to strain  $\epsilon \geq 20\%$ ) and reaches ideal strength limits in some architectures<sup>23,28,29</sup>.

To explore the extreme dynamic response of these materials, we performed microparticle impact experiments using the LIPIT method<sup>30</sup>, in which 14- $\mu\text{m}$ -diameter  $\text{SiO}_2$  spheres were accelerated by a pulsed laser to collide with the samples at velocities from  $\sim 30 \text{ m s}^{-1}$  to  $\sim 1.2 \text{ km s}^{-1}$ . This choice of projectiles created a difference of about one order of magnitude between the particle diameter and the unit cell size, enabling us to maintain a proper separation of scales. The impact event was captured through a microscope objective using an ultrahigh frame rate camera (up to  $10^9 \text{ frames s}^{-1}$ ) allowing for measurements of the particle velocity during the collision. The post-mortem analysis of the impacted material was performed via scanning electron microscopy (SEM) and laser-confocal microscopy to assess the crater site morphology (see Methods for details).

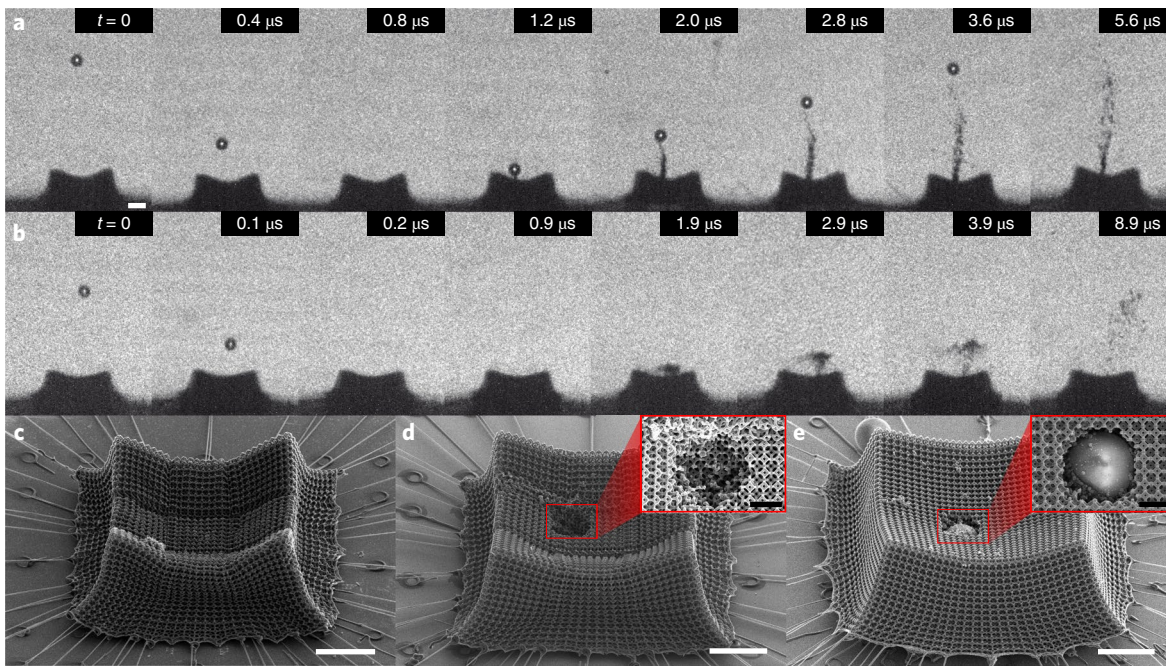


**Fig. 2 | Impact processes and resulting damage.** **a,b**, Impact onto nanoarchitected carbon materials of ~23% relative density with impact and rebound velocities of 238 and 50 m s<sup>-1</sup>, respectively (**a**), and impact velocity of 676 m s<sup>-1</sup> and particle capture (**b**). **c**, Sample of ~23% relative density after elastic impact with no permanent deformation at 50 m s<sup>-1</sup>. **d,e**, Post-impact micrographs of sample from **a** showing cratering (**d**) and sample from **b** showing a captured SiO<sub>2</sub> particle (**e**). White scale bars, 20 μm; black inset scale bars, 5 μm. The scale bar in **a** also applies to **b**.

Impacts of the SiO<sub>2</sub> particles onto the tetrakaidekahedron materials exhibited three distinct regimes: (1) elastic impact (Supplementary Video 1), (2) cratering with particle rejection (Supplementary Video 2) and (3) cratering with particle capture (Supplementary Video 3), which varied with impact energy and with the relative density of the architected carbon. In the elastic impact regime, no permanent deformation occurred and the microparticles rebounded with a high coefficient of restitution  $\alpha = |v_r|/|v_0|$ , defined as the ratio of the rebound ( $v_r$ ) and impact ( $v_0$ ) velocities. Beyond the less interesting elastic impact regime (regime 1, Fig. 2c), the cratering and particle rejection regime (regime 2) consisted of permanent deformation in the form of a localized crater and a non-zero  $\alpha$ , as shown in Fig. 2a,d. The cratering and particle capture regime (regime 3) was characterized by permanent deformation in the form of a crater, with  $\alpha = 0$  due to the particle remaining embedded inside the material, as depicted in Fig. 2b,e. Craters at both relative densities generally had a cylindrical shape, with diameters of ~15 μm and depths varying based on impact velocity, without notable spallation or fracture emanating radially from the craters for any of the probed velocities (see Extended Data Fig. 2). Close-up and cross-sectional views of the crater bases showed indications of brittle failure in the carbon struts and compaction of debris (Extended Data Fig. 3), consistent with the observed failure of other pyrolytic carbon materials in the quasi-static regime<sup>2,23</sup>.

We calculated the impact and rebound energies, defined as  $W_0 = mv_0^2/2$  and  $W_r = mv_r^2/2$ , respectively, using the velocities measured from the camera frames and defining the particle mass as  $m = 4/3\delta\pi r^3$  with density  $\delta = 1,850 \text{ kg m}^{-3}$  (microParticles GmbH) and radius  $r = 14 \mu\text{m}$ . Based on these energies, the total dissipated or inelastic energy was calculated as the difference  $W_{i,\text{tot}} = W_0 - W_r$ . Calibration impact experiments, where the SiO<sub>2</sub> microparticles were launched onto a thick Si substrate, revealed dissipation in the microparticles to contribute towards  $W_{i,\text{tot}}$ , which can be attributed to densification of SiO<sub>2</sub> occurring at the pressures associated with these impacts<sup>31</sup> (Supplementary Information section I, Extended

Data Figs. 4 and 5, Supplementary Videos 4 and 5). To decouple this contribution from the nanoarchitected material response, we define the inelastic energy due to the lattice materials alone as:

$$W_i = W_0 - W_r - W_{i,\text{SiO}_2}(W_r), \quad (1)$$

where  $W_{i,\text{SiO}_2}(W_r)$  is the inelastic energy due to consolidation in the microparticles, expressed as a fit of the inelastic energy in SiO<sub>2</sub>-Si impacts as a function of their rebound energy  $W_r$  (Supplementary Information section I and Extended Data Fig. 6). Plotting the energetics of experiments on the architected materials (Fig. 3) shows that impacts on the  $\bar{\rho} \approx 14\%$  samples exhibited cratering and rebound (regime 2) for all probed impact velocities above 50 m s<sup>-1</sup>, with full-sample penetration and substrate rebound occurring for velocities beyond ~490 m s<sup>-1</sup>, as indicated by the sharp increase in rebound velocities. The  $\bar{\rho} \approx 23\%$  samples exhibited both cratering and rebound as well as particle capture for all impact velocities beyond the elastic regime; no full-sample penetration was observed for any of the probed velocities. Partial cratering occurred at velocities below ~515 m s<sup>-1</sup> before transitioning to a capture-dominated regime that extended to velocities of up to ~820 m s<sup>-1</sup> (Fig. 3b). Using Bloch wave numerical analysis, we confirmed that the impact velocities remained below the bulk elastic wave speeds of 1,807 and 2,206 m s<sup>-1</sup> for the  $\bar{\rho} \approx 14\%$  and 23% samples, respectively, supporting that all experiments were in the same regime, where an elastic wave precursor acted on the material in addition to subsequent inelastic mechanisms<sup>32</sup>. Linear fitting of the inelastic energies for the  $\bar{\rho} \approx 14\%$  and 23% samples yielded slopes of 0.79 and 1.00, indicating an on-average ideal energy dissipation response of the denser materials in the probed regime. Despite the distinct response regimes and characteristic wave velocities for the two types of samples, similar cylindrical crater morphologies appeared in both, as shown in Extended Data Fig. 2.

For comparison with other materials under ballistic impact conditions, we calculated the specific inelastic energy in our

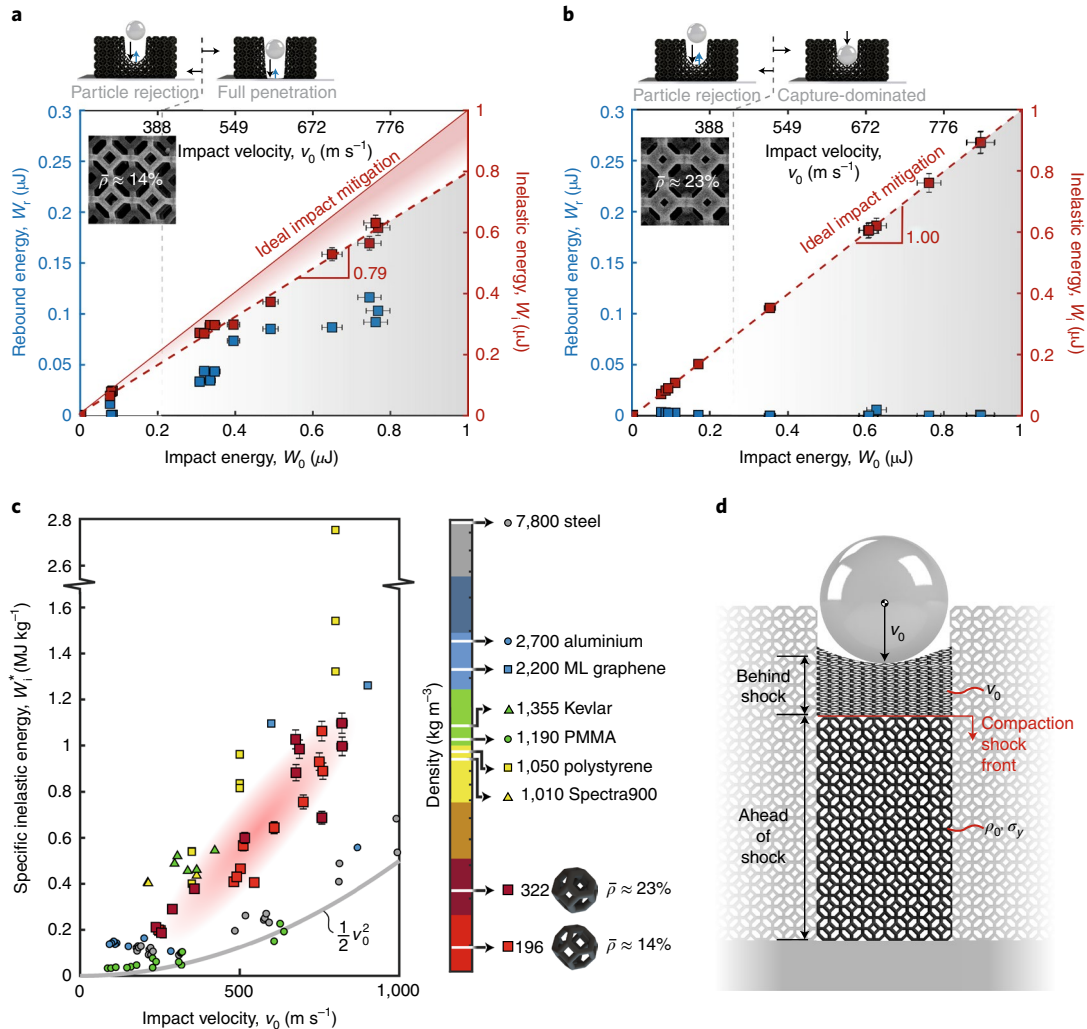


**Fig. 3 | Impact energetics and comparison to ballistic materials.** **a,b**, Impact energetics for experiments on the  $14\% \pm 3\%$  (**a**) and  $23\% \pm 4\%$  (**b**) relative density samples, exhibiting particle rejection, full penetration and particle capture regimes. Linear fits of the inelastic energy  $W_i$  as a function of the impact energy  $W_0$  are presented as red dashed lines. **c**, Comparison of mass-normalized inelastic energies  $W_i^* = W_{in}/m_p$ , where  $m_p$  is the impact participation mass (permanently deformed target material), as a function of impact velocity  $v_0$  for ballistic impact experiments at the macro- and microscale (refs. <sup>21,22,33–38</sup> detailed in Supplementary Table 1). ML, multilayer; PMMA, polymethyl methacrylate; Spectra900, woven polyethylene-fibre composite. **d**, Diagram depicting a compaction shock as an energy-dissipating mechanism in the nanoarchitected carbon samples. Colour bar in **c** corresponds to a logarithmic density scale. Error bars correspond to the standard error in measurements.

experiments— $W_i^* = W_i/m_p$ , defined as the inelastic energy normalized by the material mass that participates in inelastic deformation within the crater—and compared these values with those of other macro- and microscale impact experiments at comparable velocities (Fig. 3c). For consistency, our results are only compared with those from experiments where a spherical projectile penetrates a solid plate or layer of a material of interest, enabling the same specific inelastic energy calculation using the cylindrical volume corresponding to the projectile footprint area and the material thickness (see Supplementary Table 1 for details). Throughout the tested regime, the nanoarchitected carbon achieved specific inelastic energies of  $0.19\text{--}1.1 \text{ MJ kg}^{-1}$ , outperforming homogeneous materials such as steel<sup>33,34</sup>, aluminium<sup>35,36</sup> and polymethyl methacrylate (PMMA)<sup>37</sup>, with thicknesses ranging from  $400 \mu\text{m}$  to a few millimetres. Expressing the inelastic energy as  $W_i = \frac{1}{2}m_p v_0^2 + W_d$ , where the first term is an approximate measure of kinetic energy imparted on the deformed material and  $W_d$  accounts for dissipation mechanisms such as impact delocalization or material compaction<sup>21</sup>, hints at additional dissipation mechanisms in the carbon lattice materials

as observed in common ballistic materials such as Kevlar and Spectra fibre composites<sup>38</sup>. These materials, in contrast to the homogeneous ones, deviate from the  $\frac{1}{2}v_0^2$  trend line in Fig. 3c due to mechanisms accounted for by  $W_d$ . In the case of our nanoarchitected carbon, we found evidence of compaction shock mechanisms—known to occur in lattices and foams at even lower velocities<sup>11,17,20,32</sup>—which could account for this notable deviation (Extended Data Figs. 3 and 7). We note that while other failure mechanisms such as hydrodynamic jetting are likely to occur in conjunction with the propagation of this shock<sup>39–41</sup>, isolating their contribution from that of classical mechanisms such as strut fracture lies beyond the scope of the present study due to limitations in our experimental technique. Thus, generally following a one-dimensional shock analysis (see Fig. 3d and Supplementary Information section II for details), we arrive at an expression for the energy per unit mass expended across the shock ( $U^+$ ) of the form

$$U^+ = \frac{1}{2}v_0^2 + \frac{v_0 \sigma_y}{\rho_0(A + Bv_0)}, \quad (2)$$

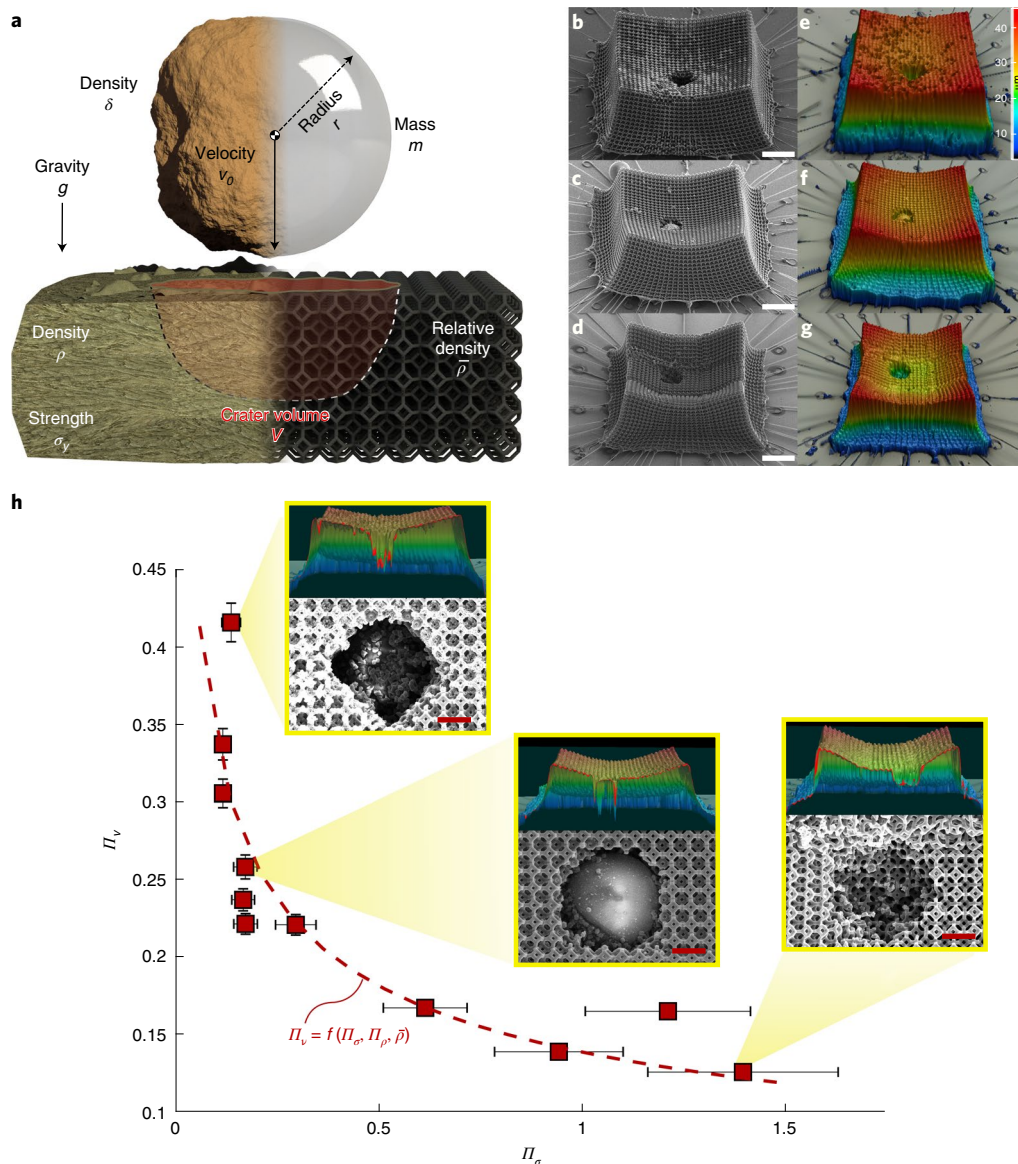


**Fig. 4 | Impact scaling laws for damage prediction.** **a**, Diagram of physical quantities associated with a planetary impact-type problem showing the analogy to the present study. **b-d**, Post-mortem SEM micrographs of a  $\bar{\rho} \approx 23\%$  sample after particle capture at  $v_0 = 757 \text{ m s}^{-1}$  (**b**) and  $v_0 = 676 \text{ m s}^{-1}$  (**c**), and particle rejection at  $v_0 = 238 \text{ m s}^{-1}$  (**d**). **e-g**, 3D confocal microscope images of the samples in **b-d** used for volumetric estimation of the craters. **h**, Cratering efficiency  $\Pi_v$  as a function of the strength dimensionless group  $\Pi_\sigma$  for the  $\bar{\rho} \approx 23\%$  samples (power-law fit shown as a dashed red line). White scale bars in **b-d**, 20  $\mu\text{m}$ ; red scale bars in **h**, 5  $\mu\text{m}$ . Error bars correspond to the standard error in measurements.

where  $\sigma_y$  is the collapse stress ahead of the shock,  $\rho_0$  is the original density of the material, and  $A$  and  $B$  are fit parameters, with the second term corresponding to the deviation from the  $\frac{1}{2}v_0^2$  trend line. As can be observed from this second term, dissipation is further enhanced by nanoscale size effects that provide this nanoarchitected carbon with an extended elastic limit<sup>23,28</sup> (Extended Data Fig. 8), enabling higher collapse stresses  $\sigma_y$  to be achieved during compaction. Compared to ballistic experiments of nanomaterial films, such as multilayer graphene and polystyrene, our experiments reveal comparable specific energies with the added benefit of having up to one order-of-magnitude lower densities of 196 and  $322 \text{ kg m}^{-3}$  for the  $\bar{\rho} \approx 14\%$  and  $23\%$  samples (with  $\rho = 1,400 \text{ kg m}^{-3}$  for pyrolytic carbon<sup>2</sup>), respectively, and without requiring nanometre-scale sample thicknesses to achieve this response. In contrast to those nanoscale films, as long as the structural length scales are maintained in thicker carbon nanoarchitected materials (that is,

consisting of a larger number of unit cell tessellations), the same mass-normalized values reported above could be attained in thicker form factors. When comparing materials across a given specific impact energy, that is,  $W_0^* = W_0/m_p$ , the nanoarchitected carbon outperformed nanoscale polystyrene by 75% and Kevlar composites by up to 72% (Extended Data Fig. 9).

To obtain predictive tools for the formation of craters upon ballistic impact, we analysed our experiments within the framework of planetary impact, a physically similar process. Despite the drastic difference in scale, both problems lack the knowledge of time-dependent stress and strain fields and instead rely on post-mortem crater analysis and prior knowledge of the projectile velocity, material properties (for example, strength and density) and gravitational acceleration. As a first-order approximation to predict the cratering response of nanoarchitected materials, we relate the volume of the crater  $V$  to the parameters associated with the

impactor (radius  $r$ , velocity  $v_0$  and density  $\delta$ ) and those of the underlying material (strength  $\sigma_y$  and density  $\rho$ ) at gravitational acceleration  $g$  (see Fig. 4a) of the type

$$V = f[\underbrace{\{r, v_0, \delta\}}_{\text{particle}}, \underbrace{\{\rho, \sigma_y\}}_{\text{target material}}, g]. \quad (3)$$

Applying the Buckingham- $\Pi$  theorem to these variables, plus accounting for porosity (that is, in the form of relative density  $\bar{\rho}$ ) in the target material, admits a total of five non-unique dimensionless groups, which are chosen to be<sup>42</sup>

$$\underbrace{\frac{\rho V}{m}}_{=\Pi_v} = \tilde{f} \left[ \underbrace{\frac{gr}{v_0^2}}_{=\Pi_g}, \underbrace{\frac{\sigma_y}{\rho v_0^2}}_{=\Pi_\sigma}, \underbrace{\frac{\rho}{\delta}}_{=\Pi_\rho}, \bar{\rho} \right]. \quad (4)$$

Here,  $\Pi_v$  represents the ratio between the mass expelled from the crater and the mass of the impactor  $m$ , that is, the cratering efficiency, which is related to a gravity term  $\Pi_g$ , a strength term  $\Pi_\sigma$ , a density term  $\Pi_\rho$  and the relative density  $\bar{\rho}$ . It is crucial to note that this analysis applies only under the condition that separation of scales between the impactor and the porosity length scales is maintained.

Approximating the impactor to behave as a point source<sup>42,43</sup>, such that energy and momentum are coupled into a volume that is small compared with other features of interest, enables us to replace the particle-related variables in equation (3) with a single measure  $C = rv_0^\mu \delta^\nu$  where the exponents  $\mu$  and  $\nu$  are specific to a given target material. Since our experiments are conducted in a strength-dominant regime with  $\sigma_y \gg \rho gr$ , which we confirm to be valid by measuring  $\sigma_y = 25 \pm 4$  MPa for our  $\bar{\rho} \approx 23\%$  materials (Extended Data Fig. 8) to be nine orders of magnitude larger than  $\rho gr$ , we can neglect the dependence on  $\Pi_g$  and obtain a power-law form<sup>43</sup> of equation (4) as

$$\Pi_v = \Pi_\sigma^{-\frac{3\mu}{2}} \Pi_\rho^{3\nu-1} f(\bar{\rho}). \quad (5)$$

For simplicity we assume  $f(\bar{\rho}) = \bar{\rho}^\gamma$ .

To analyse our results within the framework of equation (5), we obtained estimates for the crater volumes (and hence  $\Pi_v$ ) using laser confocal microscopy (Fig. 4e–g);  $\Pi_\sigma$  was estimated from nanomechanical compression experiments on representative samples with relative densities matching those of the impacted samples. Since full sample penetration occurred in the  $\bar{\rho} \approx 14\%$  samples, we restricted this analysis to the  $\bar{\rho} \approx 23\%$  samples where only partial cratering was observed. Performing a fit of the form in equation (5) yielded the trend line presented in Fig. 4h, providing good agreement on the evolution of the cratering efficiency as a function of the strength term. These experiments yielded fit parameters  $\gamma = 1.35$ ,  $\nu \approx 1/3$  and  $\mu = 0.26$ , with the latter approaching the theoretical bound  $\mu = 1/3$  for a momentum-dominated (as opposed to energy-dominated) response (that is,  $C \propto (mv_0)^{1/3}$ )<sup>43</sup>, lending it to further explorations to extend these analytical tools—and to understand the evolution of these parameters—as a function of the target material's architecture. While dimensional planetary impact analysis provides a general predictive tool for crater excavation, the propagation of compaction shock waves (and their associated mechanisms such as hydrodynamic jetting<sup>39–41</sup>) can provide the framework to understand the enhanced energy dissipation of nanoarchitected materials, supported by evidence of notable compaction within the craters (Extended Data Fig. 3). In particular, since the effective densification stress within the compaction region of the shock is a function of the quasi-static collapse strength  $\sigma_y$  (Supplementary Information section II), size effects leading to the optimal strength-to-density ratios<sup>28</sup> and extended elastic regimes (Extended Data Fig. 8) can be

tailored to further enhance and guide the design of dissipation capabilities in these materials.

In summary, we have produced a 3D nanoarchitected pyrolytic carbon that exhibits extreme energy dissipation upon supersonic microparticle impact. Its architecture and nanoscale material size effects give specific energy dissipation ~70% superior to that of Kevlar composites and nanoscale polystyrene films for the same specific impact energies. Adopting the dimensional analysis of planetary impact provided a framework for accurate damage prediction, with the potential of being applicable to dimensionally similar experiments at larger scales. Although further exploration is necessary to understand the effect of a given architecture on the cratering response, our work indicates that the ability to propagate compaction shocks can account for the additional dissipation mechanisms that give these materials their extreme impact efficiency. We see this work as a step beyond classical testing of nanoarchitected materials, venturing into unexplored mechanical regimes that are essential to the widespread applicability of architected materials. Proper understanding of architected materials in these regimes can help inform the design of protective materials for lightweight ballistic defence or space debris applications.

## Online content

Any methods, additional references, Nature Research reporting summaries, source data, extended data, supplementary information, acknowledgements, peer review information; details of author contributions and competing interests; and statements of data and code availability are available at <https://doi.org/10.1038/s41563-021-01033-z>.

Received: 14 July 2020; Accepted: 6 May 2021;

Published online: 24 June 2021

## References

- Zheng, X. et al. Ultralight, ultrastiff mechanical metamaterials. *Science* **344**, 1373–1377 (2014).
- Bauer, J., Schroer, A., Schwaiger, R. & Kraft, O. Approaching theoretical strength in glassy carbon nanolattices. *Nat. Mater.* **15**, 438–443 (2016).
- Portela, C. M. et al. Extreme mechanical resilience of self-assembled nanolabyrinthine materials. *Proc. Natl Acad. Sci. USA* **117**, 5686–5693 (2020).
- Frenzel, T., Findeisen, C., Kadic, M., Gumbsch, P. & Wegener, M. Tailored buckling microlattices as reusable light-weight shock absorbers. *Adv. Mater.* **28**, 5865–5870 (2016).
- Krödel, S. & Daraio, C. Microlattice metamaterials for tailoring ultrasonic transmission with elastoacoustic hybridization. *Phys. Rev. Appl.* **6**, 064005 (2016).
- Frenzel, T., Kadic, M. & Wegener, M. Three-dimensional mechanical metamaterials with a twist. *Science* **358**, 1072–1074 (2017).
- Meyers, M. A. *Dynamic Behavior of Materials* Ch. 5 (Wiley, 1994).
- Schaedler, T. A. et al. Designing metallic microlattices for energy absorber applications. *Adv. Eng. Mater.* **16**, 276–283 (2014).
- Dattelbaum, D. M., Ionita, A., Patterson, B. M., Branch, B. A. & Kuettner, L. Shockwave dissipation by interface-dominated porous structures. *AIP Adv.* **10**, 075016 (2020).
- Deshpande, V. S. & Fleck, N. A. High strain rate compressive behaviour of aluminum alloy foams. *Int. J. Impact Eng.* **24**, 277–298 (2000).
- Barnes, A. T., Ravi-Chandar, K., Kyriakides, S. & Gaitanaros, S. Dynamic crushing of aluminum foams: part I—experiments. *Int. J. Solids Struct.* **51**, 1631–1645 (2014).
- Yungwirth, C. J., Wadley, H. N., O'Connor, J. H., Zakrajsek, A. J. & Deshpande, V. S. Impact response of sandwich plates with a pyramidal lattice core. *Int. J. Impact Eng.* **35**, 920–936 (2008).
- Xue, Z. & Hutchinson, J. W. A comparative study of impulse-resistant metal sandwich plates. *Int. J. Impact Eng.* **30**, 1283–1305 (2004).
- Mueller, J., Matlack, K. H., Shea, K. & Daraio, C. Energy absorption properties of periodic and stochastic 3D lattice materials. *Adv. Theory Simul.* **2**, 1900081 (2019).
- Mines, R. A., Tsopanos, S., Shen, Y., Hasan, R. & McKown, S. T. Drop weight impact behaviour of sandwich panels with metallic micro lattice cores. *Int. J. Impact Eng.* **60**, 120–132 (2013).
- Harris, J. A., Winter, R. E. & McShane, G. J. Impact response of additively manufactured metallic hybrid lattice materials. *Int. J. Impact Eng.* **104**, 177–191 (2017).

17. Ozdemir, Z. et al. Energy absorption in lattice structures in dynamics: experiments. *Int. J. Impact Eng.* **89**, 49–61 (2016).
18. Tancogne-Dejean, T., Li, X., Diamantopoulou, M., Roth, C. C. & Mohr, D. High strain rate response of additively-manufactured plate-lattices: experiments and modeling. *J. Dyn. Behav. Mater.* **5**, 361–375 (2019).
19. Lai, C. Q. & Daraio, C. Highly porous microlattices as ultrathin and efficient impact absorbers. *Int. J. Impact Eng.* **120**, 138–149 (2018).
20. Hawrelak, J. A. et al. Dynamic behavior of engineered lattice materials. *Sci. Rep.* **6**, 28094 (2016).
21. Lee, J.-H., Loya, P. E., Lou, J. & Thomas, E. L. Dynamic mechanical behavior of multilayer graphene via supersonic projectile penetration. *Science* **346**, 1092–1096 (2014).
22. Hyon, J. et al. Extreme energy absorption in glassy polymer thin films by supersonic micro-projectile impact. *Mater. Today* **21**, 817–824 (2018).
23. Zhang, X., Vyatskikh, A., Gao, H., Greer, J. R. & Li, X. Lightweight, flaw-tolerant, and ultrastrong nanoarchitected carbon. *Proc. Natl Acad. Sci. USA* **116**, 6665–6672 (2019).
24. Portela, C. M., Greer, J. R. & Kochmann, D. M. Impact of node geometry on the effective stiffness of non-slender three-dimensional truss lattice architectures. *Extreme Mech. Lett.* **22**, 110–138 (2018).
25. Deshpande, V. S., Ashby, M. F. & Fleck, N. A. Foam topology: bending versus stretching dominated architectures. *Acta Mater.* **49**, 1035–1040 (2001).
26. Ashby, M. F. The properties of foams and lattices. *Phil. Trans. R. Soc. A* **364**, 15–30 (2006).
27. Evans, A. G. et al. Concepts for enhanced energy absorption using hollow micro-lattices. *Int. J. Impact Eng.* **37**, 947–959 (2010).
28. Zhang, X. et al. Theoretical strength and rubber-like behaviour in micro-sized pyrolytic carbon. *Nat. Nanotechnol.* **14**, 762–769 (2019).
29. Crook, C. et al. Plate-nanolattices at the theoretical limit of stiffness and strength. *Nat. Commun.* **11**, 1579 (2020).
30. Veysset, D. et al. Dynamics of supersonic microparticle impact on elastomers revealed by real-time multi-frame imaging. *Sci. Rep.* **6**, 25577 (2016).
31. Schill, W., Heyden, S., Conti, S. & Ortiz, M. The anomalous yield behavior of fused silica glass. *J. Mech. Phys. Solids* **113**, 105–125 (2018).
32. Lind, J., Jensen, B. J., Barham, M. & Kumar, M. In situ dynamic compression wave behavior in additively manufactured lattice materials. *J. Mater. Res.* **34**, 2–19 (2019).
33. Dean, J., Dunleavy, C. S., Brown, P. M. & Clyne, T. W. Energy absorption during projectile perforation of thin steel plates and the kinetic energy of ejected fragments. *Int. J. Impact Eng.* **36**, 1250–1258 (2009).
34. Yungwirth, C. J., O'Connor, J., Zakraysek, A., Deshpande, V. S. & Wadley, H. N. Explorations of hybrid sandwich panel concepts for projectile impact mitigation. *J. Am. Ceram. Soc.* **94**, 62–75 (2011).
35. Golsdsmith, W. & Finnegan, S. A. Penetration and perforation processes in metal targets at and above ballistic velocities. *Int. J. Mech. Sci.* **13**, 843–866 (1971).
36. Gupta, N. K., Iqbal, M. A. & Sekhon, G. S. Experimental and numerical studies on the behavior of thin aluminum plates subjected to impact by blunt- and hemispherical-nosed projectiles. *Int. J. Impact Eng.* **32**, 1921–1944 (2006).
37. Abbud, L. H., Talib, A. R., Mustapha, F., Tawfique, H. & Najim, F. A. Behaviour of transparent material under high velocity impact. *Int. J. Mech. Mater. Eng.* **5**, 123–128 (2010).
38. Lee, B. L. et al. Penetration failure mechanisms of armor-grade fiber composites under impact. *J. Compos. Mater.* **35**, 1605–1633 (2001).
39. Lind, J., Robinson, A. K. & Kumar, M. Insight into the coordinated jetting behavior in periodic lattice structures under dynamic compression. *J. Appl. Phys.* **128**, 015901 (2020).
40. Branch, B. et al. Controlling shockwave dynamics using architecture in periodic porous materials. *J. Appl. Phys.* **121**, 135102 (2017).
41. Branch, B. et al. A comparison of shockwave dynamics in stochastic and periodic porous polymer architectures. *Polymer* **160**, 325–337 (2019).
42. Housen, K. R. & Holsapple, K. A. Impact cratering on porous asteroids. *Icarus* **163**, 102–119 (2003).
43. Housen, K. R., Sweet, W. J. & Holsapple, K. A. Impacts into porous asteroids. *Icarus* **300**, 72–96 (2018).

**Publisher's note** Springer Nature remains neutral with regard to jurisdictional claims in published maps and institutional affiliations.

© The Author(s), under exclusive licence to Springer Nature Limited 2021

## Methods

**Fabrication of nanoarchitected carbon materials.** Creation of the nanoarchitected materials began with fabrication of an architected polymeric precursor material, made of IP-Dip photoresist, in two-photon lithography Photonic Professional GT system (Nanoscribe). Using a  $10\text{ }\mu\text{m}$  tetrakaidecahedron unit cell, a  $30 \times 30 \times 15$  tessellation was fabricated by stitching  $10 \times 10 \times 1$  domains using a mechanical stage, with a laser power of  $17.5\text{ mW}$  and a scan speed of  $10\text{ mm s}^{-1}$ . Planning for subsequent high-temperature processing, we used silicon substrates and fabricated the materials on top of an elastic foundation with the purpose of mechanically decoupling the precursor material from the substrate and avoid warping (Extended Data Fig. 1). This elastic foundation consisted of an array of vertically aligned helical springs made of IP-Dip resist which were connected to the substrate at the bottom and the precursor material at the top. For a  $300 \times 300\text{ }\mu\text{m}$  footprint material, we utilized nine helical springs per  $100 \times 100\text{ }\mu\text{m}^2$  section, each with a beam radius  $r = 2.6\text{ }\mu\text{m}$ , helix radius  $r_h = 5\text{ }\mu\text{m}$ , pitch  $\lambda = 7\text{ }\mu\text{m}$  and height  $h = 28\text{ }\mu\text{m}$  (Extended Data Fig. 1). To anchor the precursor sample to the substrate, one spring in the central  $100 \times 100\text{ }\mu\text{m}^2$  section was replaced by a  $10\text{-}\mu\text{m}$ -radius monolithic pillar. All samples were developed for  $4\text{ h}$  in propylene glycol monomethyl ether acetate, followed by a  $10\text{ min}$  rinse in isopropyl alcohol, and subsequent drying in a critical point dryer (Autosamdry 931, Tousimis).

Upon drying, the samples were pyrolysed in a vacuum furnace (OTF-1500, MTI) fitted with a 4-inch-diameter quartz tube. The process consisted of a hold at  $900^\circ\text{C}$  for  $5\text{ h}$ , with constant heating and cooling rates of  $10^\circ\text{C min}^{-1}$ . An initial pressure at room temperature of  $50\text{ mtorr}$  or less was required to ensure minimal sample warping during the pyrolysis process. The final carbon materials underwent linear isotropic shrinkage of  $75\%$ , resulting in unit cell sizes of  $2.5 \pm 0.2\text{ }\mu\text{m}$ , and beam diameters ranging between  $d = 370 \pm 40$  and  $530 \pm 40\text{ nm}$ .

**LIPIT setup.** High-velocity impacts were performed with the LIPIT method<sup>21,22,30</sup>. Using LIPIT, single microparticles were accelerated from a launch pad towards the target and directly observed via high-speed imaging. The launch pad was a glass substrate ( $210\text{ }\mu\text{m}$  thick,  $25\text{ mm}$  diameter, Corning No. 2 microscope cover slip) with a sacrificial gold layer ( $60\text{ nm}$  thick, sputter coated) and a polyurea layer ( $30\text{ }\mu\text{m}$  thick, spin coated). Before performing an experiment, microparticles were deposited onto the polyurea surface and mechanically distributed with ethanol and lens cleaning paper. Immediately before acceleration, a single microparticle was selected. A high-energy excitation laser pulse (pulsed Nd:YAG,  $532\text{ nm}$  wavelength,  $10\text{ ns}$  duration) was then focused onto the gold layer directly beneath the particle, resulting in local ablation of the gold film, expansion of the polyurea layer and subsequent acceleration of the selected particle. Particle velocity was varied by tuning the excitation laser pulse energy. The particle trajectory and target region was illuminated with a second laser pulse (Cavilux, Specialized Imaging,  $640\text{ nm}$  wavelength,  $30\text{ }\mu\text{s}$  duration) and imaged through a microscope objective by an ultrahigh-speed camera (SIMX16, Specialised Imaging) consisting of 16 independently triggered intensified charge-coupled devices. From the image sequence, impact and rebound velocities were measured and subsequent behaviours observed.

**Quasi-static nanomechanical compression experiments.** To obtain the static mechanical properties of the nanoarchitected carbon materials, we fabricated representative  $10 \times 10 \times 10$  tessellations of the tetrakaidecahedron architecture with relative density  $\bar{\rho} = 20\% \pm 1\%$  (approximating the  $\bar{\rho} = 23\% \pm 3\%$  dynamic samples), and performed *in situ* nanomechanical compression experiments. Following the pyrolysis step, the samples remained supported by a sacrificial central pillar, which was designed to fail upon the initial loading regime to allow proper contact between the substrate and the sample (Extended Data Fig. 8). A minimum of seven samples per configuration were compressed in a custom nanomechanical instrument inside an SEM chamber (Quanta 200 FEG, Thermo Fisher), which provided load–displacement data along with real-time observation of the experiment at quasi-static strain rates of  $\dot{\epsilon} = 10^{-3}\text{ s}^{-1}$ . The load–displacement data were converted to stresses and strains by normalizing by the sample footprint area and height, respectively. Since pillar failure did not occur at the same point for all samples, zero-strain was defined to be the start of the test for consistency.

All samples exhibited a linear loading regime once proper contact was established, with some sporadic settling events, as well as brittle, catastrophic

failure. The majority of samples exhibited an elastic regime, beyond pillar collapse, on the order of  $\epsilon \approx 10\%$ . The settling events and brittle failure are both depicted as sudden strain bursts (that is, horizontal lines with few data points) in the stress–strain response presented in Extended Data Fig. 8. This response was used to compute the effective Young's modulus and strength, which were defined as the slope of the linear response after pillar collapse and the maximum stress before catastrophic failure, respectively. An effective Young's modulus of  $0.43 \pm 0.09\text{ GPa}$  was obtained, which is consistent with the values reported in the literature<sup>2,23</sup> when accounting for the difference in architecture and relative density compared with the samples in those works. We also calculated an effective strength value of  $25 \pm 4\text{ MPa}$ , expectedly lower than those reported for octet carbon nanolattices<sup>2,23</sup>.

**Elastic wave velocity calculation.** To estimate the elastic wave speeds of the nanoarchitected carbon materials, we computed the dispersion relation for the two relative densities tested experimentally (COMSOL Multiphysics). The geometries were meshed using linear tetrahedral elements. We employed Bloch wave analysis and focused on the long-wavelength limit to estimate the longitudinal and shear wave speeds of each geometry.

**Confocal microscopy for crater volume determination.** To estimate the crater volumes, we performed 3D laser confocal microscopy (Keyence VK-X250) on the post-mortem samples, which provided a nanometre-resolution 3D reconstruction of the samples as shown in Fig. 4e–g. Using the Keyence MultiFileAnalyzer software, we obtained volumetric measurements of each crater. For sloped surfaces, the crater volume was estimated as the average between the volumes measured from the highest and lowest crater-edge points. Compacted debris at the bottom of the craters (if applicable) was taken to be the crater base. For the case of embedded microparticles, the crater volume was corrected to account for the fraction of the microparticle below the surface.

## Data availability

The data supporting the findings of this study are available within this article and its Supplementary Information.

## Acknowledgements

C.M.P. and D.M.K. acknowledge financial support from Office of Naval Research Award N00014-16-1-2431. J.R.G. acknowledges support from the Vannevar Bush Faculty Fellowship. D.V., Y.S. and K.A.N. acknowledge support by the US Army Research Office through the Institute for Soldier Nanotechnologies (ISN), under Cooperative Agreement Number W911NF-18-2-0048. The authors thank W. J. Schill for valuable discussions.

## Author contributions

C.M.P., D.V., K.A.N., D.M.K. and J.R.G. designed the study and interpreted the results. C.M.P. and B.W.E. fabricated the samples and conducted nanomechanical experiments. D.V. and Y.S. performed the impact experiments. C.M.P. and B.W.E. analysed all data. C.M.P., K.A.N. and J.R.G. supervised the project. C.M.P., D.M.K. and J.R.G. wrote the manuscript with input from all authors.

## Competing interests

The authors declare no competing interests.

## Additional information

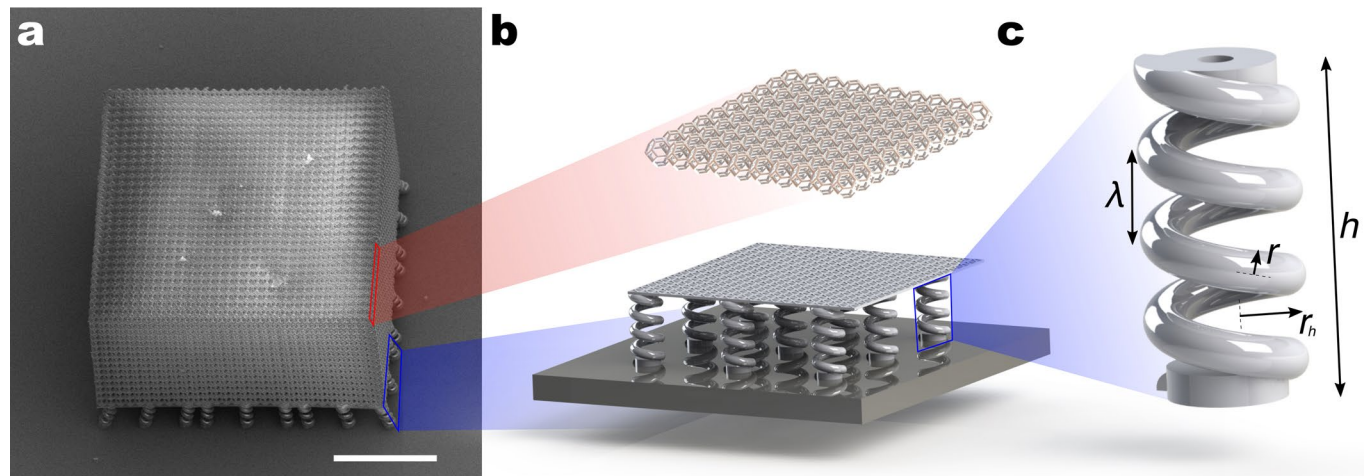
Extended data are available for this paper at <https://doi.org/10.1038/s41563-021-01033-z>.

**Supplementary information** The online version contains supplementary material available at <https://doi.org/10.1038/s41563-021-01033-z>.

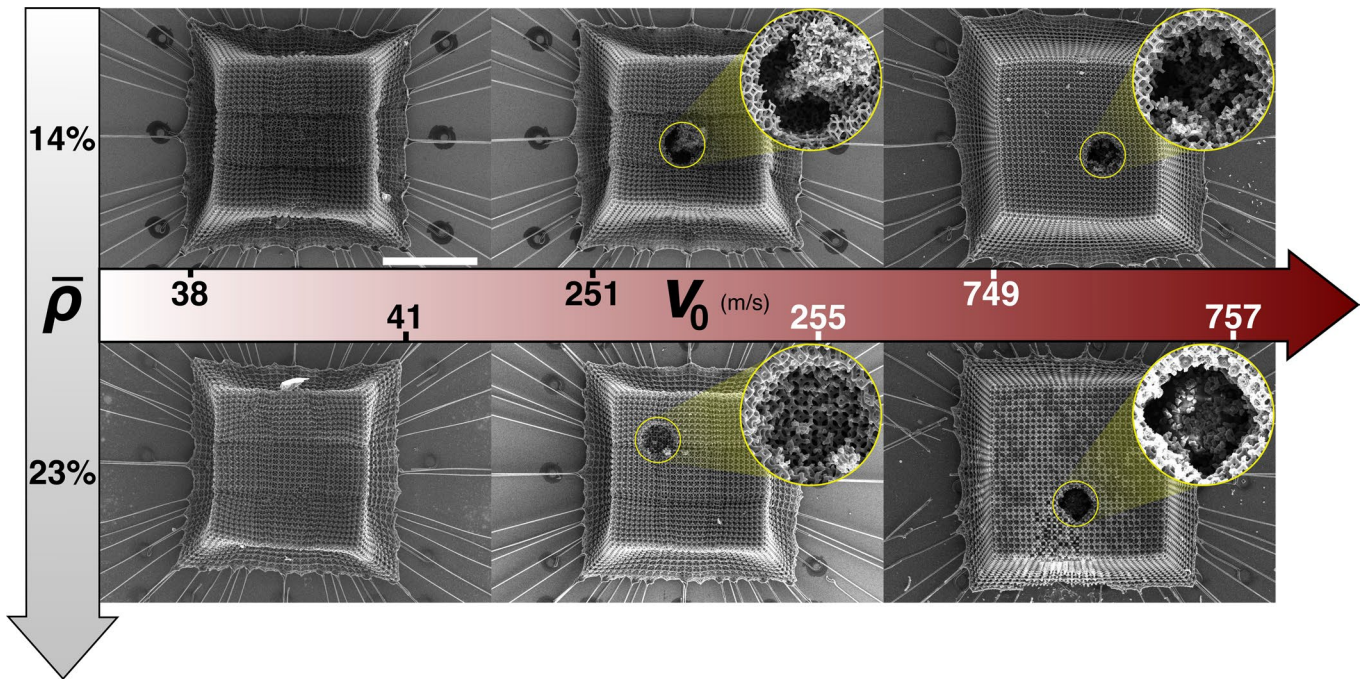
**Correspondence and requests for materials** should be addressed to C.M.P. or J.R.G.

**Peer review information** *Nature Materials* thanks the anonymous reviewers for their contribution to the peer review of this work.

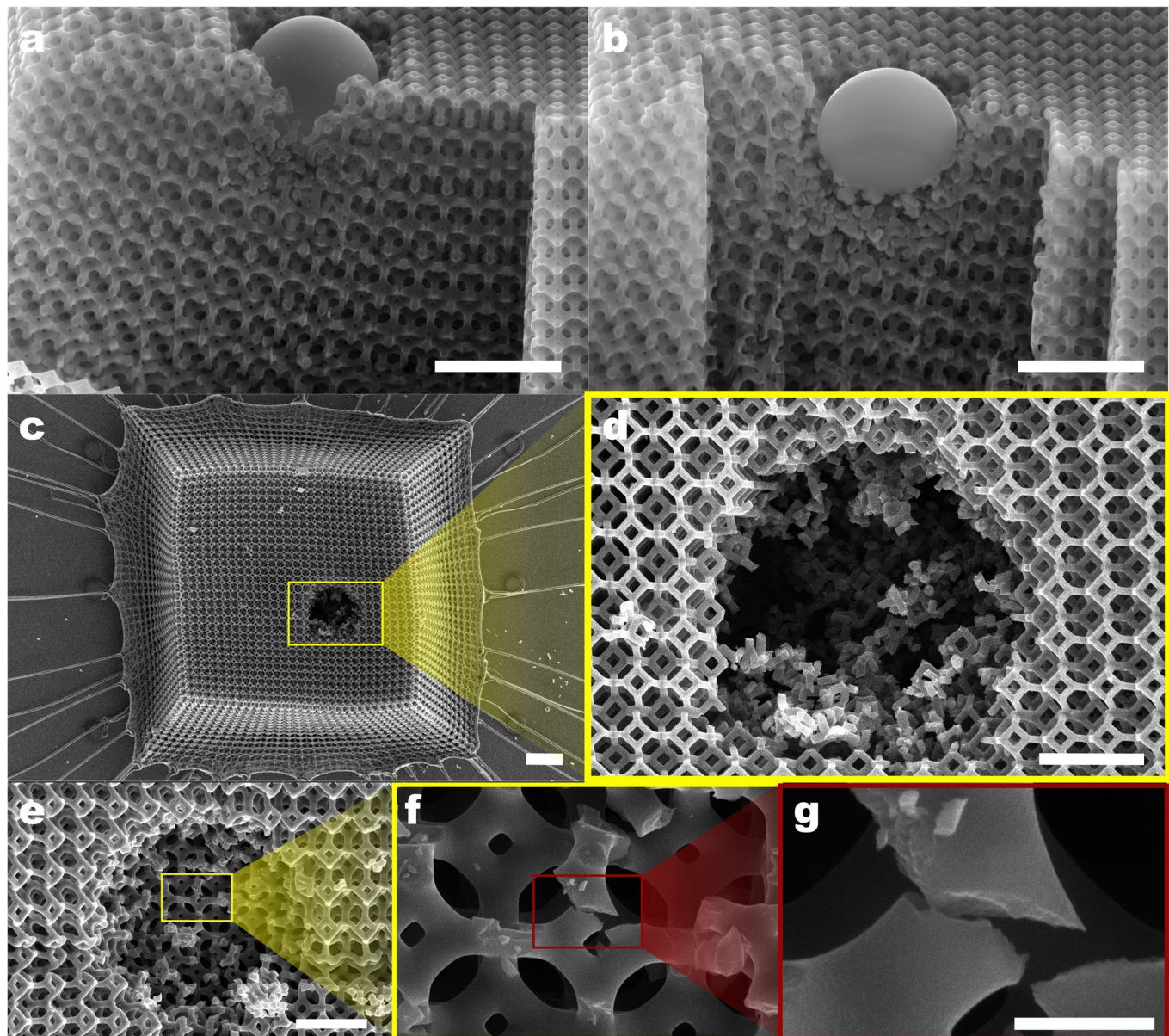
**Reprints and permissions information** is available at [www.nature.com/reprints](http://www.nature.com/reprints).



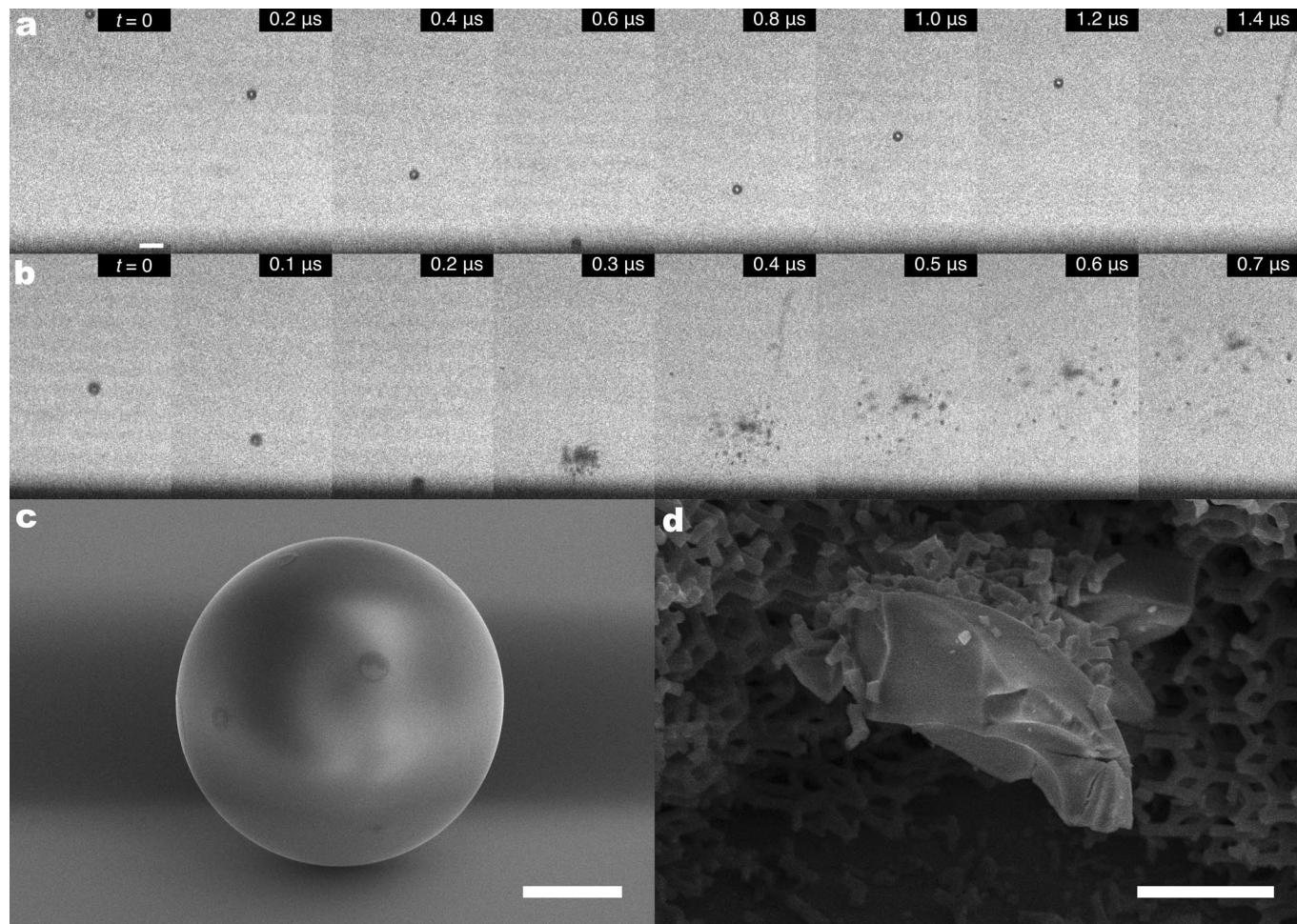
**Extended Data Fig. 1 | Pre-pyrolysis sample configuration.** **a**, Polymeric IP-Dip tetrakaidecahedron sample with overall dimensions of  $300 \times 300 \times 150 \mu\text{m}^3$ . **b**, Diagram of spring elastic foundation decoupling unit cells from the Si substrate, and **c**, detailed view of a single helical spring with its characteristic parameters (see Methods for values). Scale bar,  $100 \mu\text{m}$ .



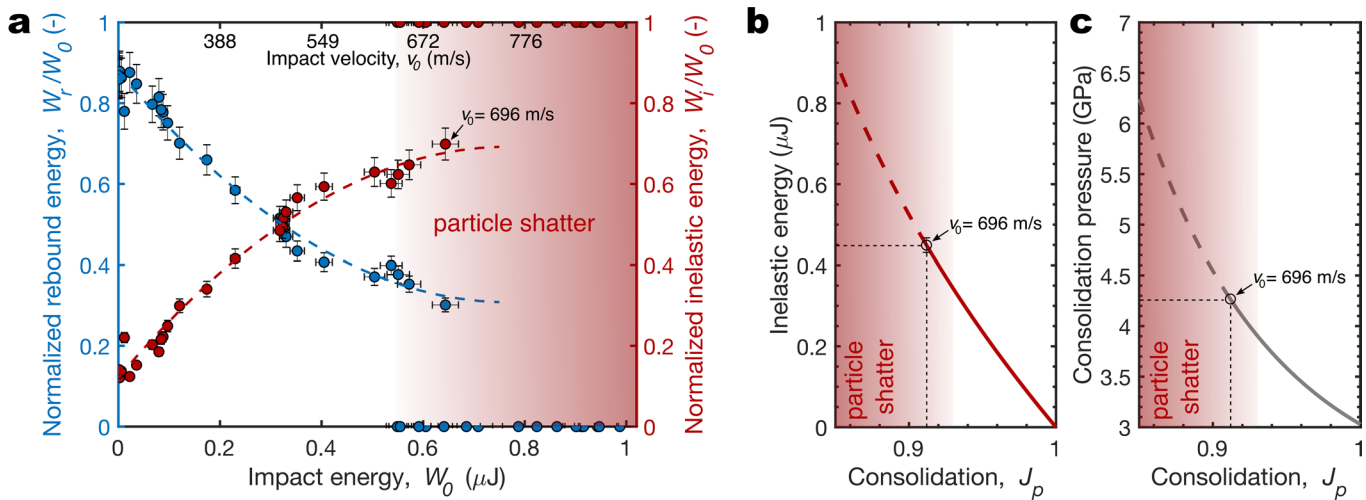
**Extended Data Fig. 2 | Crater morphology evolution.** Crater evolution as a function of relative density  $\bar{\rho}$  and impact velocity  $v_0$ . Full penetration of the  $\bar{\rho} \approx 14\%$  sample was observed for the impact at 749 m/s, and deep particle embedding was observed in the  $\bar{\rho} \approx 23\%$  sample at 757 m/s. White scale bar 40  $\mu\text{m}$ , inset diameters 18  $\mu\text{m}$ .



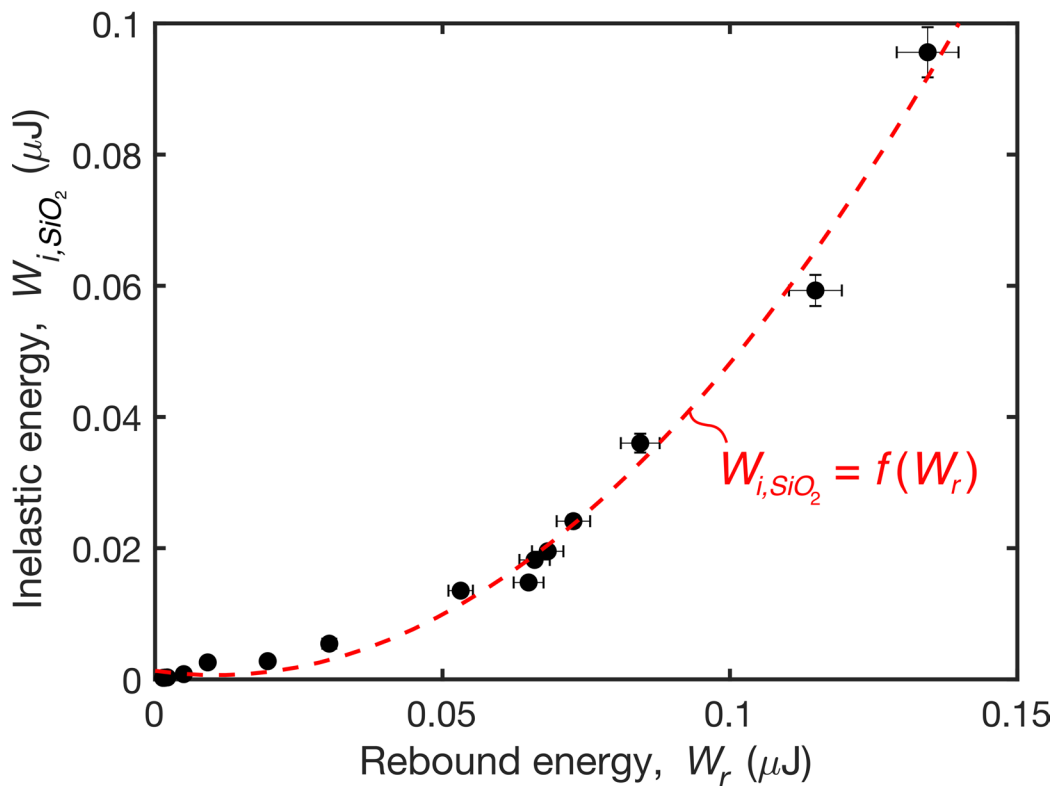
**Extended Data Fig. 3 | Material compaction and failure in craters.** **a**, FIB cross-section at the edge of the crater (and captured projectile) of a  $\bar{\rho} \approx 23\%$  sample after impact at  $v_0 = 516$  m/s. **b**, FIB cross-section at the middle of the crater for the sample in **a**, showing compacted unit cells below the captured projectile. **c,d**, Crater of a  $\bar{\rho} \approx 14\%$  sample after impact at  $v_0 = 749$  m/s exhibiting full-sample penetration and particle rebound at  $v_r = 296$  m/s. Some compacted unit cells are observed to remain within the crater. **e-g**, Crater of a  $\bar{\rho} \approx 23\%$  sample after impact at  $v_0 = 255$  m/s and particle rebound at  $v_r = 48$  m/s, showing brittle failure of individual carbon struts. Scale bars in **a-c**, 10  $\mu\text{m}$ ; **d,e**, 5  $\mu\text{m}$ ; and **g**, 500 nm.



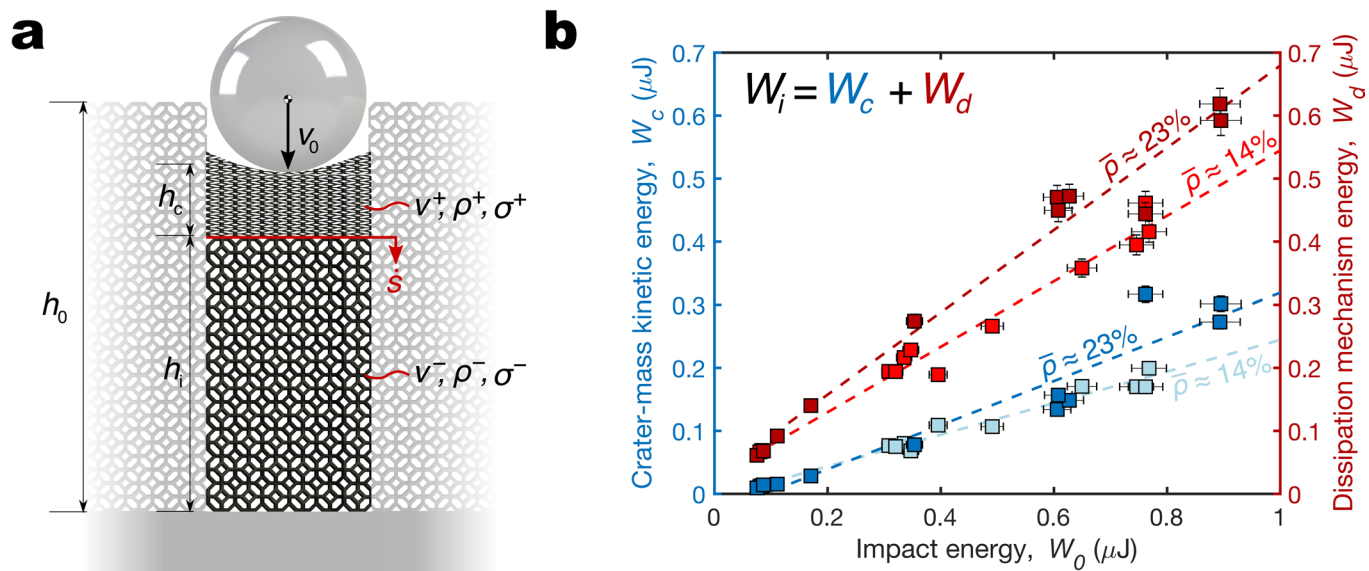
**Extended Data Fig. 4 |  $\text{SiO}_2$ -Si impact experiments.** Impact of  $14 \mu\text{m}$ -diameter  $\text{SiO}_2$  spheres onto a Si substrate. **a**, Impact and rebound speeds of  $514 \text{ m/s}$  and  $339 \text{ m/s}$ , respectively, and **b**, impact speed of  $646 \text{ m/s}$  causing particle shatter. **c**, Micrograph of initial  $\text{SiO}_2$  particle, and **d**, fragment of a shattered particle. Scale bar in **a,b**,  $30 \mu\text{m}$ ; **c,d**,  $4 \mu\text{m}$ .



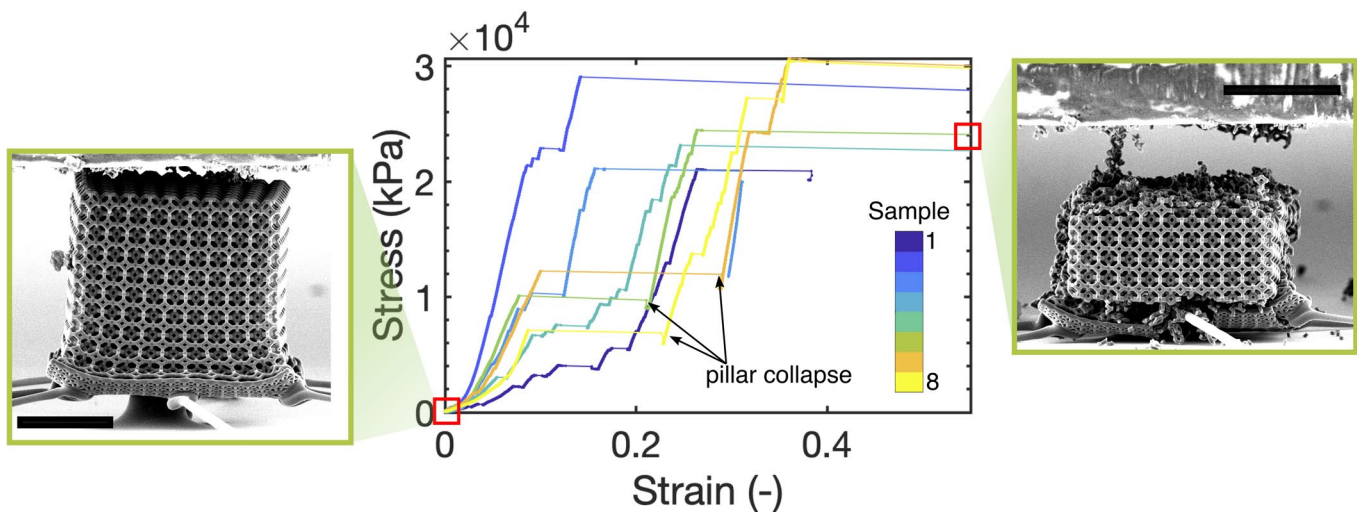
**Extended Data Fig. 5 | SiO<sub>2</sub>-Si impact energetics.** **a**, Normalized rebound ( $W_r/W_0$ ) and inelastic ( $W_i/W_0$ ) energies, as functions of the impact energy ( $W_0$ ), exhibiting a nonlinear increase in dissipation with increasing impact energy and a transition to a particle shatter regime between 650–700 m/s. Particle shatter was categorized as a normalized inelastic energy of 1. **b**, Inelastic energy as a function of average particle consolidation  $J_p$ , that is, the resulting fraction of the original volume after impact, estimated using the model proposed by Schill et al.<sup>31</sup>. The transition to the shatter regime is estimated to occur for an average  $J_p$  of 0.91–0.93. These values serve as a lower bound for the actual consolidation in the particles since consolidation is most likely localized in some regions of the particle rather than being constant throughout the entirety of the volume. **c**, Estimated consolidation pressure as a function of  $J_p$ , obtained from the model by Schill et al.<sup>31</sup>. Error bars correspond to the standard error in measurements.



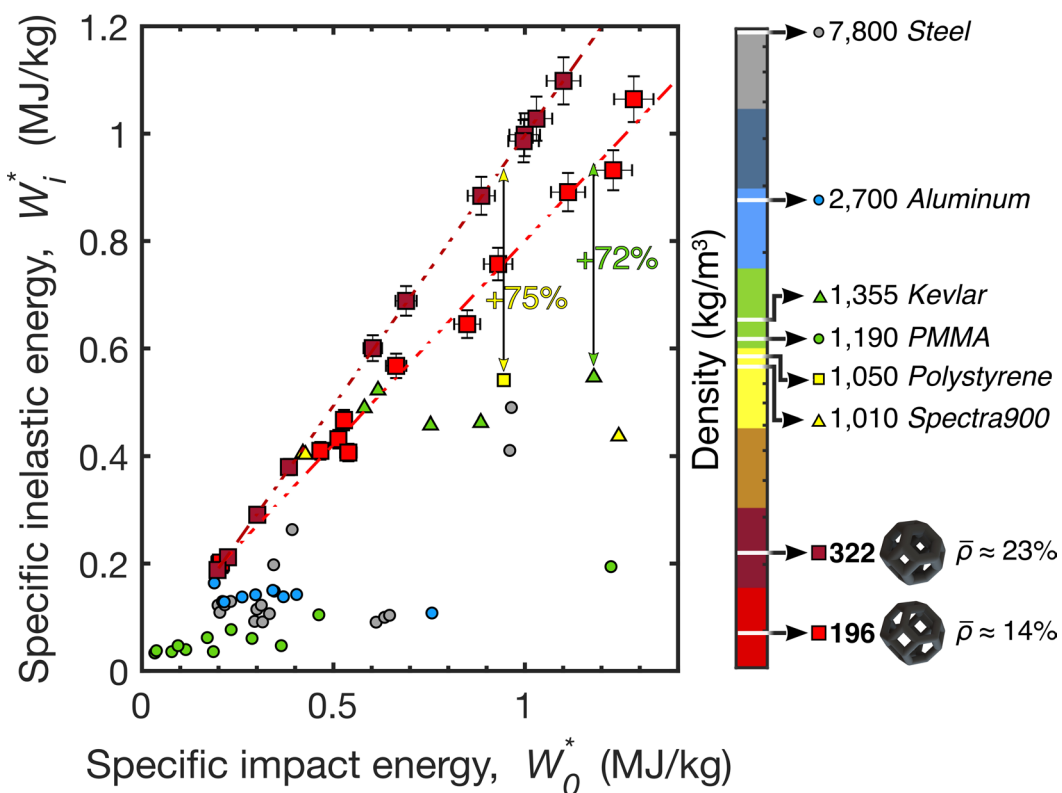
**Extended Data Fig. 6 | SiO<sub>2</sub> inelastic energy function.** Inelastic energy from the SiO<sub>2</sub>-Si impact experiments as a function of the rebound energy, restricted to the range of rebound energies observed in the nanoarchitected carbon impact experiments. A quadratic function of the form  $W_{i,SiO_2} = C_1 W_r^2 + C_2 W_r + C_3$ , with fit parameters  $C_1 = 5.94 \times 10^{-6}$ ,  $C_2 = -0.126$ , and  $C_3 = 1.34 \times 10^{-9}$ , was used to estimate the inelastic energy contribution of the SiO<sub>2</sub> projectiles in the nanoarchitected carbon impact experiments. This first-order approximation assumes that comparable SiO<sub>2</sub> dissipation occurs during rebound from compacted nanoarchitected carbon compared to the Si substrate. This function was used to isolate the contribution of the nanoarchitected carbon to the inelastic energy in the impact experiments. Error bars correspond to the standard error in measurements.



**Extended Data Fig. 7 | Energy dissipation via compaction shocks.** **a**, Diagram of a compaction shock front propagating within a cylindrical crater, caused by impact at velocity  $v_0$ , where the shock front (moving at velocity  $\dot{s}$ ) is shown in red. The particle velocity  $v$ , density  $\rho$ , and stress  $\sigma$  behind and ahead of the discontinuity are depicted using +/- superscripts, respectively. **b**, Inelastic energy of the nanoarchitected carbon impact experiments, as a function of the impact energy  $W_0$ , decomposed as  $W_i = W_c + W_d$ . Here,  $W_c = m_p v_0^2 / 2$  corresponds to a measure of the kinetic energy imparted on the participation mass (that is, the crater-mass kinetic energy), and  $W_d$  is the energy attributed to other dissipation mechanisms such as compaction shock propagation. This decomposition is in line with the form presented in Eq. (2). For the same impact energy  $W_0$ , a higher  $W_d$  value is observed in the  $\bar{\rho} \approx 23\%$  compared to the  $\bar{\rho} \approx 14\%$  samples. Error bars correspond to the standard error in measurements.



**Extended Data Fig. 8 | Nanomechanical compression experiments.** Uniaxial in situ compression of  $\bar{\rho} = 20 \pm 1\%$  relative density samples, with insets showing a representative sample before and after compression. After an extended elastic strain limit on the order of 10% (consistent with other nanoscale pyrolytic carbon explorations<sup>23,28</sup>), catastrophic brittle failure was observed upon reaching a collapse stress level. All samples were fabricated on a sacrificial pillar which collapsed at low loads to enable proper sample contact with the substrate. Zero-strain was defined as the beginning of the experiment for consistency. Scale bars,  $10 \mu\text{m}$ .



**Extended Data Fig. 9 | Specific impact energy comparison.** Comparison of the specific inelastic energy  $W_i^* = W_i/m_p$ , that is, the inelastic energy normalized by the participation mass, attained by the nanoarchitected carbon materials compared to other materials with specific impact energies  $W_0^* = W_0/m_p$  in the same experimental regime. The nanoarchitected carbon samples were observed to outperform nanoscale polystyrene<sup>22</sup> and Kevlar composites<sup>38</sup> by 75% and 72%, respectively, for the same specific impact energy. Error bars correspond to the standard error in measurements.